

Solving Constrained Optimization Problems Using Hybrid Qubit-Qumode Quantum Devices

Rishab Dutta,¹ Brandon Allen,¹ Nam P. Vu,^{1,2,3} Chuzhi Xu,¹ Kun Liu,⁴ Fei Miao,⁵ Bing Wang,⁵ Amit Surana,⁶ Chen Wang,⁷ Yongshan Ding,^{4,8,9} and Victor S. Batista^{1,9}

¹*Department of Chemistry, Yale University, New Haven, CT, USA 06520*

²*Department of Chemistry, Lafayette College, Easton, PA, USA 18042*

³*Department of Electrical and Computer Engineering, Lafayette College, Easton, PA, USA 18042*

⁴*Department of Computer Science, Yale University, New Haven, CT, USA 06520*

⁵*School of Computing, University of Connecticut, Storrs, CT, USA 06269*

⁶*RTX Technology Research Center, East Hartford, CT, USA 06118*

⁷*Department of Physics, University of Massachusetts-Amherst, Amherst, MA, USA 01003*

⁸*Department of Applied Physics, Yale University, New Haven, CT, USA 06520*

⁹*Yale Quantum Institute, Yale University, New Haven, CT, USA 06511*

Optimization challenges span a wide array of fields, from logistics and scheduling to finance, materials science, and drug discovery. Among these, Quadratic Unconstrained Binary Optimization (QUBO) problems are especially significant due to their computational complexity and their potential as a key application for quantum computing. In this work, we introduce an approach for solving QUBO problems using hybrid qubit-qumode bosonic quantum computers—devices that manipulate and measure the quantum states of light within microwave cavity resonators. We map problems with soft and hard constraints onto the Hamiltonian of a hybrid quantum system, consisting of a single qubit coupled to multiple qumodes. The optimal solution is encoded in the ground state of the system, which is revealed by photon-number measurements. Trial states are prepared through universal qubit-qumode circuits, employing echoed conditional displacement (ECD) gates in combination with qubit rotations. Our approach demonstrates the immense potential of hybrid quantum systems, showcasing their ability to efficiently tackle complex optimization problems in both academia and industry.

I. INTRODUCTION

Variational Quantum Algorithms (VQAs) are a class of hybrid methods that combine quantum and classical computing to address optimization problems. They are particularly well-suited for near-term quantum devices, which face constraints such as limited qubit counts and high error rates^{1–4}. VQAs can address a wide range of real-world applications. These include molecular property prediction and generation^{5,6}, RNA folding problems⁷, and protein-ligand docking⁸. They can also be applied to training machine learning models⁹, solving structural design¹⁰, vehicle routing¹¹, and capital-budgeting problems¹². VQAs are designed to approximate the ground states of Hamiltonians that encode optimization problems. Among the most prominent VQAs are the Quantum Approximate Optimization Algorithm (QAOA)^{13,14} and the Variational Quantum Eigensolver (VQE)^{2,3,15}. QAOA constructs parameterized quantum circuit (PQC) ansatzes by using the Hamiltonian itself. VQE, on the other hand, iteratively updates the parameters of an ansatz to minimize an expectation value computed with a classical computer.

In this work, we demonstrate how to implement VQAs for solving constrained optimization problems using hybrid qubit-qumode quantum devices. Our approach employs variational echoed conditional displacement (ECD) ansatzes^{16–18}, after transforming the optimization tasks into quadratic unconstrained binary optimization (QUBO) problems^{19,20}. We demonstrate the

capabilities of the method as compared to QAOA in solving a Binary Knapsack Problem (BKP)²¹. In solving the BKP problem, we demonstrate that the VQE approach utilizing the ECD ansatz on a hybrid qubit-qumode device outperforms the standard QAOA method implemented with qubits. This finding is consistent with recent studies^{22–25} which reveal the inherent limitations of QAOA and the importance of developing more effective methods for addressing combinatorial optimization problems.

Quantum devices built with a combination of qubits and bosonic qumodes represent a new paradigm toward quantum computing^{26–32}. Qumodes are quantum harmonic oscillators and the Fock basis of qumodes can have countably infinite discrete levels in principle³³, instead of only two levels in the case of qubits. Quantum algorithms based on qumodes can be more resourceful in tackling multiple variables with fewer quantum information building blocks, leading to the development of qumode-based combinatorial optimization algorithms^{34–37}. These algorithms so far have focused on the qumode-only hardware architecture based on photonic quantum computing^{38–40}, where non-Gaussian quantum gates such as cubic phase gates that are necessary for universality can be challenging to implement⁴¹. In contrast, coupling one or multiple qumodes with a qubit can efficiently implement the universal gate sets for both qumodes and the composite qubit-qumode system^{16–18,42,43}. In the circuit quantum electrodynamics (cQED) approach, this can be achieved by coupling microwave cavities with a trans-

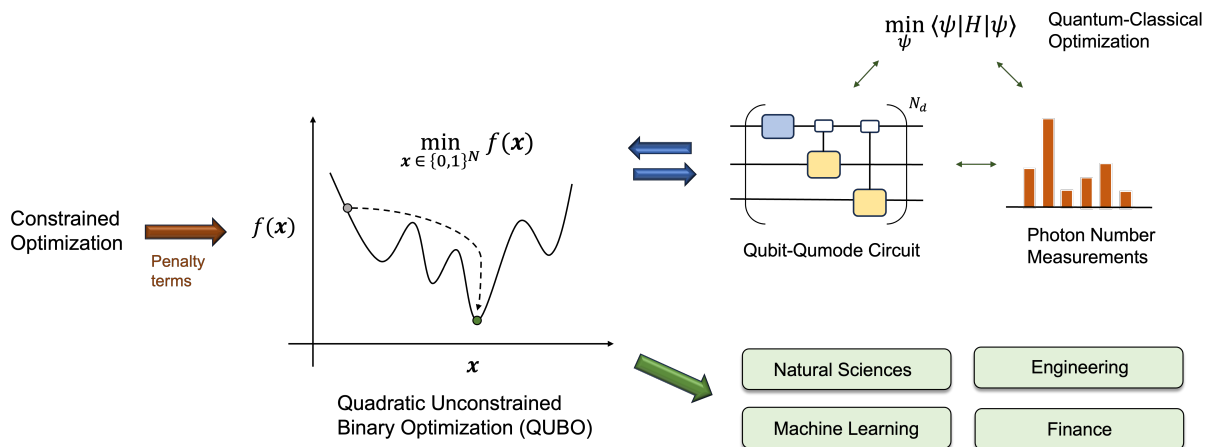


FIG. 1. A constrained optimization problem is transformed into a QUBO problem, which is then solved by a qubit-qumode device. The QUBO problem, which has a diverse range of applications, is transformed into a problem of finding the ground state of qubit-qumode Hamiltonian. The ground state is represented by a parameterized quantum circuit involving qubit-qumode gates and the cost function is computed by measuring photon numbers inside the qumodes.

mon qubit^{26,28}, which has been recently shown to achieve quantum error correction beyond break-even for logical qubits⁴⁴ and qudits⁴⁵. Another unique feature of hybrid qubit-qumode devices is its native gates such as the qubit-conditioned bosonic displacement operator that allows exploring a different optimization space when used for PQC in variational methods¹⁸, which leads to deep circuits if emulated on a qubit-only device^{30,46}.

We demonstrate a method for solving optimization problems with both soft and hard constraints using quantum hardware that integrates qumodes with a qubit. The computational task is framed as a quadratic unconstrained binary optimization (QUBO) problem^{19,20}, with the Hilbert space of the multi-qubit Hamiltonian mapped onto the combined Hilbert spaces of a single qubit and a multi-qumode device. Measurements in the computational basis of the multi-qubit Hamiltonian are translated into photon number measurements of the qumodes. The optimal binary solution is then reconstructed from photon number measurements on the hybrid qubit-qumode system, using the bosonic ECD-VQE ansatz⁴⁷ generated by qubit-qumode ECD gates combined with qubit rotations, as schematically shown in Figs. 1 and 3.

The rest of this paper is organized as follows. In Section II, we discuss how to map a constrained optimization problem into a qubit-qumode Hamiltonian and how to solve it using a hybrid quantum-classical variational approach. We apply our method to two different optimization problems in Section III. In Section IV, we analyze how noise can affect performance, before concluding in Section V.

II. METHODS

In this section, we review how to represent a constrained optimization problem in terms of a qubit Hamil-

tonian before discussing how to implement it on a qubit-qumode device. Then we introduce a variational approach to find the optimal solution as the ground state of the qubit Hamiltonian.

A. Qubit Hamiltonian

Let us review how to transform a constrained optimization problem into a QUBO form with the binary knapsack problem (BKP), a fundamental integer programming problem in combinatorial optimization and operations research²¹. It can be defined as

$$\max_{\mathbf{x}} V = \sum_{j=0}^{N_0-1} v_j x_j, \quad x_j \in \{0, 1\}, \quad (1a)$$

$$\text{subject to } W_0(\mathbf{x}) = \sum_{j=0}^{N_0-1} w_j x_j \leq W, \quad (1b)$$

where W is the total weight capacity of a knapsack, N_0 is the number of items available, $\{v_j\}$ are the item values, and $\{w_j\}$ are the item weights. The BKP defined in Eq. (1) is also called the 0-1 knapsack problem, and is known to belong to the NP-hard computational complexity class⁴⁸⁻⁵⁰. Many real-world optimization problems can be represented as a BKP⁵¹, such as molecular drug discovery⁵².

The constrained optimization of Eq. (1) can be transformed to an unconstrained problem by introducing auxiliary binary variables $\{y_j\}$ to have a QUBO representation^{19,20}

$$\min_{\mathbf{x}, \mathbf{y}} E = -V(\mathbf{x}) + \lambda \left[W - W_0(\mathbf{x}) - \sum_{j=0}^{N_1-1} 2^j y_j \right]^2, \quad (2)$$

where λ is the quadratic penalty weight and the sum of $N_1 = \lceil \log_2(W+1) \rceil$ terms. We can now write the cost function $E(\mathbf{x})$ as a function of $\{x_j\}$ variables where the number of binary variables has increased to $N_0 + N_1$ including the auxiliary variables

$$\min_{\mathbf{x}} E = - \sum_{j=0}^{N_0-1} v_j x_j + \lambda \left[W - \sum_{j=0}^{N_0-1} w_j x_j - \sum_{j=N_0}^{N_0+N_1-1} 2^{j-N_0} x_j \right]^2, \quad (3)$$

which can now be mapped to a qubit Hamiltonian H_Q of $N = N_0 + N_1$ qubits by substituting each $x_j \mapsto \frac{1}{2}(\mathbb{I}_j - Z_j)$, where \mathbb{I} and Z are the identity and the Pauli-Z operators and the subscript index represent the qubit site. The binary variable to qubit operator mapping can be easily justified by noting that the eigenstates of the Z operator are the qubit basis states $|0\rangle$ and $|1\rangle$ with eigenvalues $+1$ and -1 , respectively. The multi-qubit Hamiltonian can then be written as

$$H_Q = - \sum_{j=0}^{N_0-1} \frac{v_j}{2} (\mathbb{I}_j - Z_j) + \lambda \left[W - \sum_{j=0}^{N_0-1} \frac{w_j}{2} (\mathbb{I}_j - Z_j) - \sum_{j=N_0}^{N_0+N_1-1} 2^{j-N_0-1} (\mathbb{I}_j - Z_j) \right]^2. \quad (4)$$

The binary string \mathbf{x}^* representing the optimal solution of Eq. (3) is now encoded into a tensor product of N computational basis states

$$|\psi\rangle = |x_0^*\rangle \otimes \cdots \otimes |x_{N-1}^*\rangle, \quad (5)$$

and is the ground state of H_Q . Similar to the BKP problem discussed above, any constrained optimization problem can be represented by a Hamiltonian H_Q of the form defined in Eq. (4) by representing the constraints by auxiliary variables and designing a quadratic penalty function.

B. Hilbert space mapping

Let us define a N -qubit Hamiltonian H_D below that can be written as a linear combination of terms each consisting of only identity and Pauli-Z operators

$$H_D = \sum_{\mu=1}^{N_H} g_{\mu} \sigma_1^{(\mu)} \otimes \cdots \otimes \sigma_N^{(\mu)} = \sum_{\mu=1}^{N_H} g_{\mu} \mathcal{D}_N^{(\mu)}, \quad (6)$$

where $\sigma_j = \mathbb{I}, Z$, the Hamiltonian coefficients $\{g_{\mu}\}$ are known, and the number of terms N_H is assumed to be a computationally manageable finite number. For example, H_Q defined in Eq. (4) consists of $\mathcal{O}(N_0^2 + N_1^2 + N_0 N_1)$ terms. Each of the $\mathcal{D}_N^{(\mu)}$ terms is a diagonal operator since

$$\mathbb{I} = |0\rangle\langle 0| + |1\rangle\langle 1|, \quad (7a)$$

$$Z = |0\rangle\langle 0| - |1\rangle\langle 1|. \quad (7b)$$

Our goal is to compute $\langle \psi | \mathcal{D}_N^{(\mu)} | \psi \rangle$ for a given state using a combination of Pauli-Z measurements on a qubit and photon number measurements on qumodes. The photon number measurements compute the probabilities of finding the discrete Fock states $\{|n\rangle\}_{n \in \mathbb{N}}$ of a quantum harmonic oscillator or number of photons in an optical mode, and are the eigenstates of the bosonic number operator, $\hat{n} |n\rangle = \hat{a}^\dagger \hat{a} |n\rangle = n |n\rangle$, where \hat{a}^\dagger, \hat{a} are bosonic creation and annihilation operators, respectively. For a realistic setup, the maximum number of photons can be set to finite integer $L-1$, where L is called the Fock cutoff. From the Fock basis perspective, a qumode is thus equivalent to a multilevel generalization of a qubit in L dimensions, also known as a qudit⁵³.

Let us first discuss it in the context of photon number measurements of one qumode for the sake of simplicity. The observable $\langle \psi | \mathcal{D}_N^{(\mu)} | \psi \rangle$ can be computed from the histogram of all possible binary strings $|q_1, \dots, q_N\rangle_Q$ from Pauli-Z measurements since

$$\langle \psi | Z_{p_1} \cdots Z_{p_N} | \psi \rangle = \sum_{\mathbf{b}} (-1)^{\sum_{i=1}^N b_{p_i}} \mathbb{P}(\mathbf{b}), \quad (8)$$

where $\{\mathbf{b}\}$ represent all qubit basis states as bitstrings, $\mathbb{P}(\mathbf{b})$ is the probability of measuring the state $|\mathbf{b}\rangle$ in the measurements, and $\sum_{i=1}^N b_{p_i}$ is the sum of the bit values at positions $\{p_1, \dots, p_N\}$, which determines the sign for each qubit in the Pauli word. Each of the binary bitstrings of N qubits can be in principle mapped to the Fock space of a single qumode with $L = 2^N$ using the binary mapping

$$|q_1, \dots, q_N\rangle_Q \leftrightarrow |n\rangle_B, \quad (9)$$

where $n = 2^0 q_1 + \dots + 2^{N-1} q_N$. Thus, the histogram of binary strings can be generated by photon number measurements on a single qumode instead of Pauli-Z measurements on multiple qubits. A single qumode Hilbert space with a realistic cutoff L can only handle mapping a few qubits realistically. However, we can expand the Hilbert space significantly by working with multiple qumodes, thus allowing the map of a large number of qubits with fewer qumodes by a constant factor $\log_2(L)$. In this work, we will focus on a hardware setup with one qubit and two qumodes, which can be readily generalized to multiple qumodes. Thus, we will explore partitioning the N -qubit Hilbert space such that it matches with the combined Hilbert space of one qubit and two qumodes, i.e., $2^N = 2 \times L_1 \times L_2$, where L_1 and L_2 are the Fock cutoffs for the first and second qumodes, respectively. Thus, the N -qubit state $|q_1, \dots, q_N\rangle_Q$ Hilbert space can now be partitioned into three pieces and mapped to

$$\begin{aligned} & |q_1\rangle_Q \otimes |q_2, \dots, q_{N-j}\rangle_Q \otimes |q_{N-j+1}, \dots, q_N\rangle_Q \\ & \leftrightarrow |q_1\rangle_Q \otimes |n\rangle_B \otimes |m\rangle_B, \end{aligned} \quad (10)$$

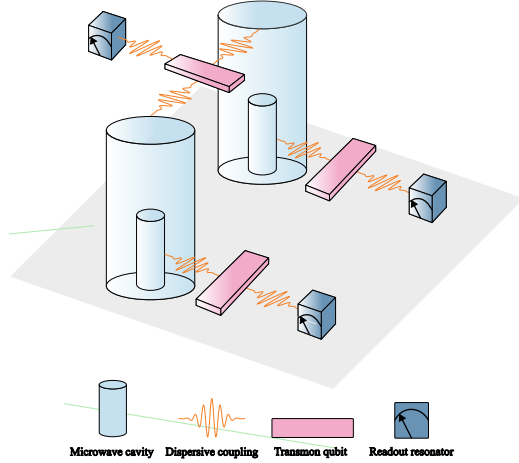


FIG. 2. Schematic to implement quantum nondemolition (QND) approach for photon number measurements for two qumodes with computational measurements for the coupled qubit. Two microwave cavities are dispersively coupled to a coupler transmon qubit with a readout resonator for computational basis measurement of the coupler qubit. Each of the cavities are also coupled to an ancillary transmon qubit with a readout resonator which allows for photon number detection followed by the approach discussed in Ref. 46.

where $1 \leq j \leq N-2$. For example, one possible partition for the Hamiltonian H_Q defined in Eq. (4) can be that the N_0 primary variables are represented by the qubit and the first qumode, whereas the second qumode represents the N_1 auxiliary variables. Let us discuss with a simple example where a one-qubit two-qumode quantum state $|\psi\rangle$ is prepared followed by Pauli-Z measurement on the qubit and photon number measurements on the two qumodes. Let us also assume $|\psi\rangle$ is originally representing a five-qubit Hamiltonian, which has been partitioned such that the first qubit remains the same, where the rest of the four qubits are grouped into two equal parts and each mapped to one qumode. The measured bitstrings of the first subsystem remains the same, i.e., $|0\rangle$ and $|1\rangle$. For each of the second and third subsystems, the possible bitstrings can be mapped as

$$|0\rangle \otimes |0\rangle_Q \mapsto |0\rangle_B, \quad |0\rangle \otimes |1\rangle_Q \mapsto |1\rangle_B, \quad (11a)$$

$$|1\rangle \otimes |0\rangle_Q \mapsto |2\rangle_B, \quad |1\rangle \otimes |1\rangle_Q \mapsto |3\rangle_B. \quad (11b)$$

For example, the one-qubit two-qumode basis state $|1\rangle_Q \otimes |3\rangle_B \otimes |2\rangle_B$ is same as the five-qubit basis state $|1, 1, 1, 1, 0\rangle_Q$.

A novel characteristic of our approach is the use of photon number measurements to output positive integers that can be easily converted to binary strings for evaluating the expectation value of the qubit-based Hamiltonian H_Q as defined in Eq. (6) or H_D of Eq. (4). Photon number measurements can be implemented using the

quantum nondemolition (QND) method, as described in Ref. 46. The QND measurement relies on the dispersive coupling between the cavity mode and its ancillary transmon qubit. In the dispersive regime, the transition frequency of the transmon qubit shifts depending on the photon number in the cavity. This shift enables the transmon to encode information about the cavity's photon state. A sequence of numerically optimized control pulses is applied to the transmon to extract this information. These pulses selectively drive the transmon between its quantum states based on the binary representation of the photon number. The transmon state carrying photon number information is probed via a dispersive readout. This QND scheme achieves high resolution and fidelity, resolving photon numbers up to 15 in single-shot experiments.⁴⁶ We refer the reader to Figure 2 for a schematic of the hardware setup where photon number measurements on two qumodes is combined with computational basis measurements on a qubit.

While computing the expectation values of the Hamiltonian in binary basis is a generally effective strategy, we may also rewrite the auxiliary binary variables $\{y_j\}$ in Eq. (2) in the basis of the photon number cutoff L of the qubits. As an example, we can use one integer variable b ,

$$\min_{\mathbf{x}, \mathbf{y}} E = -V(\mathbf{x}) + \lambda \left[W - W_0(\mathbf{x}) - b \right]^2, \quad (12)$$

such that it has values $b = 0, \dots, 2^{N_1} - 1$. By representing the integer variable to the bosonic number operator $b \mapsto \hat{n}$, we can now map the qubit Hamiltonian H_Q defined in Eq. (4) to a qubit-qumode Hamiltonian of the form

$$H_Q \mapsto H_{QB} = - \sum_{j=0}^{N_0-1} \frac{v_j}{2} (\mathbb{I}_j - Z_j) + \lambda \left[W - \sum_{j=0}^{N_0-1} \frac{w_j}{2} (\mathbb{I}_j - Z_j) - \hat{n} \right]^2, \quad (13)$$

where the number operator \hat{n} is assumed to have the Fock cutoff $L = 2^{N_1} - 1$ and the corresponding qumode represents all of the auxiliary variables. This ensures that the photon number measurements corresponding to the Hilbert space of the auxiliary variables can be used directly without the integer-to-binary mapping, and which can also lead to fewer Hamiltonian terms compared to the qubit-only Hamiltonian defined in Eq. (4).

Finally, it is also possible to represent and evaluate the Hamiltonian directly in the basis of the experimental qubit-qumode device in the projection operator form

$$H_Q \mapsto H_B = \sum_{i \in \{Q, B1, B2\}} \sum_{n=0}^{L_i} C_n^i \mathbb{P}_n^{(i)} + \sum_{i \neq j} \sum_{i, j \in \{Q, B1, B2\}} \sum_{n=0}^{L_i} \sum_{m=0}^{L_j} C_{n,m}^{i,j} \mathbb{P}_n^{(i)} \otimes \mathbb{P}_m^{(j)} \quad (14)$$

where $\mathbb{P}_n^{(i)} \equiv |n\rangle\langle n|$ is defined in the Hilbert space of the qubit mode ($i = Q$) of dimension 2 or the bosonic modes ($i = B_1$ or B_2) of dimension L_1 or L_2 . $\{C_n^i\}$ and $\{C_{n,m}^{i,j}\}$ can be deduced by rewriting the single- or two-qubit Pauli Z operators in the qubit Hamiltonian Eq. (4) following the qubit-to-qumode mapping. For example, given the mapping Eq. (11), we have $Z_2 Z_3 = |0\rangle\langle 0| - |1\rangle\langle 1| - |2\rangle\langle 2| + |3\rangle\langle 3|$. We note that for a large problem with many qubits and qumodes, the number of terms in the Hamiltonian will only grow quadratically with the number of modes.

C. Variational quantum eigensolver

We take a variational quantum eigensolver (VQE) approach to find the approximate ground state of the diagonal Hamiltonian H_D defined in Eq. (6) by optimizing the following cost function

$$\min_{\psi} E = \langle \psi | H_D | \psi \rangle = \sum_{\mu=1}^{N_H} g_{\mu} \langle \psi | \mathcal{D}_N^{(\mu)} | \psi \rangle, \quad (15)$$

where $\mathcal{D}_N^{(\mu)}$ can be computed using a qubit-qumode device following the steps below.

- Prepare a normalized trial one-qubit two-qumode state $|\psi\rangle$ using a parameterized quantum circuit.
- Generate the histogram of $|q\rangle_Q \otimes |n\rangle_B \otimes |m\rangle_B$ using Pauli-Z measurements on the qubit and photon number measurements on the two qumodes.⁴⁶
- Compute the expectation value by combining Eq. (8) and Eq. (10).

The trial state $|\psi\rangle$ can be generated by a parameterized one-qubit two-qumode circuit acting on the vacuum state

$$|\psi(\mathbf{v})\rangle = U(\mathbf{v}) \left(|0\rangle_Q \otimes |0\rangle_C \otimes |0\rangle_C \right), \quad (16)$$

where the vector \mathbf{v} represents all the circuit parameters. The parameters can be updated by optimizing Eq. (15) on a classical computer. The histograms on the qubit-qumode compute the following probabilities

$$S_{q,n,m} = |\langle q, n, m | \psi \rangle|^2, \quad (17)$$

where $q = \{0, 1\}$, $n = \{0, 1, \dots, L_1 - 1\}$, and $m = \{0, 1, \dots, L_2 - 1\}$ are the possible basis states. After repeating the measurement experiments for a finite number of times, a distribution for $\{S_{q,n,m}\}$ can be generated for computing the expectation values.

The overlaps $\{S_{q,n,m}\}$ also measure how close the approximate ground state $|\psi\rangle$ — a state in a superposition of multiple solution strings — is to the optimal solution string. Thus, for the QUBO problems, we only care about the resolution of the distribution generated by the measurements $\{S_{q,n,m}\}$ instead of how close the

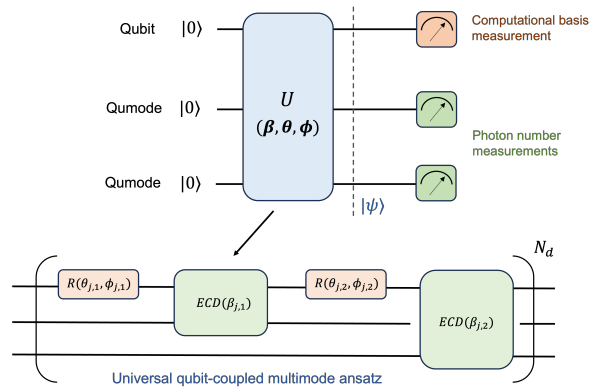


FIG. 3. Hybrid one-qubit two-qumode circuit followed by measurements for computation of expectation values of a diagonal Hamiltonian as defined in Eq. (6). The circuit consists of echoed conditional displacement (ECD) qubit-qumode gate with one-qubit rotations, as discussed in Section II C.

trial energy E is to the true ground state energy of the Hamiltonian H_D . The quantum superposition of $|\psi\rangle$ also highlights the potential advantage of quantum optimization algorithms. The parameterized trial state one-qubit two-qumode can be generically represented as

$$|\psi(\mathbf{v})\rangle = \sum_{q \in \{0,1\}} \sum_{n=0}^{L_1-1} \sum_{m=0}^{L_2-1} \lambda_{q,n,m}(\mathbf{v}) |q, n, m\rangle, \quad (18)$$

and the optimization steps depend on the gradient for the cost function defined in Eq. (15)

$$\frac{\partial E}{\partial \mathbf{v}} = \left\langle \frac{\partial \psi}{\partial \mathbf{v}} \middle| H_D | \psi \right\rangle + \left\langle \psi \middle| H_D \frac{\partial \psi}{\partial \mathbf{v}} \right\rangle, \quad (19)$$

which in turn updates $|\psi(\mathbf{v})\rangle$ for the next iteration based on Eq. (16). This means at each optimization step all the combinatorial number of basis state coefficients affect the variational parameters which in turn updates all the basis state coefficients at the same time in the next iteration. This can be hard to mimic using a classical distribution that only samples from a subspace of the full Hilbert space^{54–56}. Nevertheless, the true potential of quantum superposition is achieved when the parameterized circuit for $|\psi(\mathbf{v})\rangle$ is sufficiently expressive, which we discuss below in the context of qubit-controlled bosonic qumode gates.

The parameterized circuit for the trial state defined in Eq. (16) must be a universal ansatz for the one qubit and multiple qumodes, which can be achieved in multiple ways^{16–18,42,43}. We explore a universal ansatz based on the following circuit here¹⁷

$$U(\mathbf{v}) = U_{ER}(\beta_{N_d}, \theta_{N_d}, \phi_{N_d}) \cdots U_{ER}(\beta_1, \theta_1, \phi_1). \quad (20)$$

The building block unitaries U_{ER} are built from one-qubit arbitrary rotations

$$R(\theta, \phi) = e^{-i(\theta/2)} [\cos(\phi)X + \sin(\phi)Y], \quad (21)$$

and two one-qubit one-qumode echoed conditional displacement (ECD) operations¹⁶

$$U_{ER}(\boldsymbol{\beta}_j, \boldsymbol{\theta}_j, \boldsymbol{\phi}_j) = ECD_{0,2}(\beta_{j,2}) R_0(\theta_{j,2}, \phi_{j,2}) \\ \times ECD_{0,1}(\beta_{j,1}) R_0(\theta_{j,1}, \phi_{j,1}), \quad (22a)$$

$$ECD_{0,1}(\beta_1) = \sigma_0^- D_1(\beta_1/2) + \sigma_0^+ D_1(-\beta_1/2), \quad (22b)$$

$$ECD_{0,2}(\beta_2) = \sigma_0^- D_2(\beta_2/2) + \sigma_0^+ D_2(-\beta_2/2), \quad (22c)$$

where $D(\beta) = e^{\beta \hat{a}^\dagger - \beta^* \hat{a}}$ is the qumode displacement operator, X, Y are Pauli matrices, and $\sigma^+ = |0\rangle\langle 1|$, $\sigma^- = |1\rangle\langle 0|$ are the qubit transition operators. The operator subscripts in Eq. (22) represent the indexing for qubit and the two qumodes and tensor product is assumed. Other choices for universal ansatz include selective number-dependent arbitrary phase (SNAP) with displacement and beamsplitters^{30,42}, and conditional-not displacement gates⁴³. The variables $\{\boldsymbol{\beta}, \boldsymbol{\theta}, \boldsymbol{\phi}\}$ in Eq. (20) are matrices of dimensions $N_d \times 2$, where the complex-valued $\boldsymbol{\beta}$ matrix can also be split into two real-valued matrices of same dimensions. We call the number of blocks N_d in Eq. (20) as the depth of the universal ECD-rotation circuit. Thus, the packed vector \mathbf{v} representing all the real-valued parameters has $8N_d$ dimensions. The full circuit is illustrated in Figure 3.

III. APPLICATIONS

We now have all the tools needed to implement the ECD-VQE method for finding the ground state of a diagonal H_B . We show the applications of our ECD-VQE approach with two specific examples here.

A. Binary knapsack problem

Let us discuss a simple binary knapsack problem. Let us assume we have $N_0 = 4$ items with their values and weight constraints given by

$$\max_{\mathbf{x}} \quad 2x_0 + 5x_1 + 7x_2 + 3x_3, \quad (23a)$$

$$\text{subject to} \quad 2.5x_0 + 3x_1 + 4x_2 + 3.5x_3 \leq 7. \quad (23b)$$

Following the discussions in Section II A, the above optimization can be recast as the following QUBO problem

$$\min_{\mathbf{x}} E = -(2x_0 + 5x_1 + 7x_2 + 3x_3) \\ + \lambda \left[7 - (2.5x_0 + 3x_1 + 4x_2 + 3.5x_3) \right]^2 \\ - (x_4 + 2x_5 + 4x_6) \quad (24)$$

consisting of $4 + 3 = 7$ binary variables. For the penalty weight $\lambda = 2$, the corresponding seven-qubit Hamiltonian

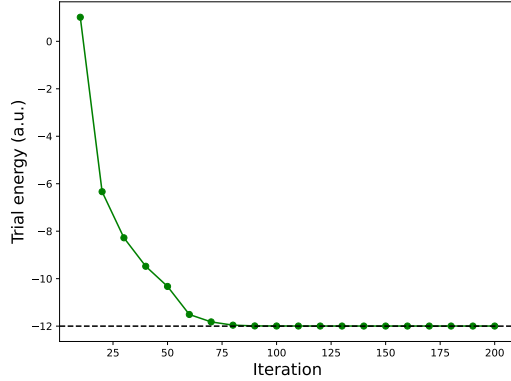


FIG. 4. Trial energy values defined in Eq. (15) at different ECD-VQE iterations while finding the ground state of H_Q defined in Eq. (25). The horizontal black line represents the exact ground state energy. The circuit depth for the trial state is $N_d = 5$.

is given by

$$H_Q = 41.75 - 14.0 Z_0 - 15.5 Z_1 - 20.5 Z_2 - 19.5 Z_3 \\ - 6.0 Z_4 - 12.0 Z_5 - 24.0 Z_6 + 7.5 Z_0 Z_1 + 10.0 Z_0 Z_2 \\ + 8.75 Z_0 Z_3 + 2.5 Z_0 Z_4 + 5.0 Z_0 Z_5 + 10.0 Z_0 Z_6 \\ + 12.0 Z_1 Z_2 + 10.5 Z_1 Z_3 + 3.0 Z_1 Z_4 + 6.0 Z_1 Z_5 \\ + 12.0 Z_1 Z_6 + 14.0 Z_2 Z_3 + 4.0 Z_2 Z_4 + 8.0 Z_2 Z_5 \\ + 16.0 Z_2 Z_6 + 3.5 Z_3 Z_4 + 7.0 Z_3 Z_5 + 14.0 Z_3 Z_6 \\ + 2.0 Z_4 Z_5 + 4.0 Z_4 Z_6 + 8.0 Z_5 Z_6. \quad (25)$$

The ground state of H_Q obtained by exact diagonalization is $|0, 1, 1, 0\rangle_Q \otimes |0, 0, 0\rangle_Q$ with eigenvalue -12. Indeed, the optimal solution is $\mathbf{x}^* = (0, 1, 1, 0)$ with the corresponding weight = 7 and value = 12. We will now partition the seven-qubit Hamiltonian into three parts such that it will be mapped to a one-qubit two-qumode system with the Fock cutoff for each qumode being $L = 8$. In other words, we map the first four qubits corresponding to the primary variables to the qubit along with the first qumode, and the rest to the second qumode. The ground state of H_Q is now mapped as

$$|0, 1, 1, 0\rangle_Q \otimes |0, 0, 0\rangle_Q \leftrightarrow |0\rangle_Q \otimes |6\rangle_C \otimes |0\rangle_C, \quad (26)$$

or in shorthand, $|0, 6, 0\rangle$. This is the state that we are after for this model benchmark system.

We show the trial energies for the ECD-VQE method applied to H_Q of Eq. (25) in Figure 4. The circuit depth chosen for the trial state is $N_d = 5$. We emulated the expectation values classically using the QuTiP Python library⁵⁷ and optimized the energy function of Eq. (15) using the Broyden–Fletcher–Goldfarb–Shanno (BFGS) algorithm as implemented in the SciPy Python library⁵⁸. It is clear from Figure 4 that the ECD-VQE method discussed here practically converges to the exact ground state energy in approximately 100 iterations.

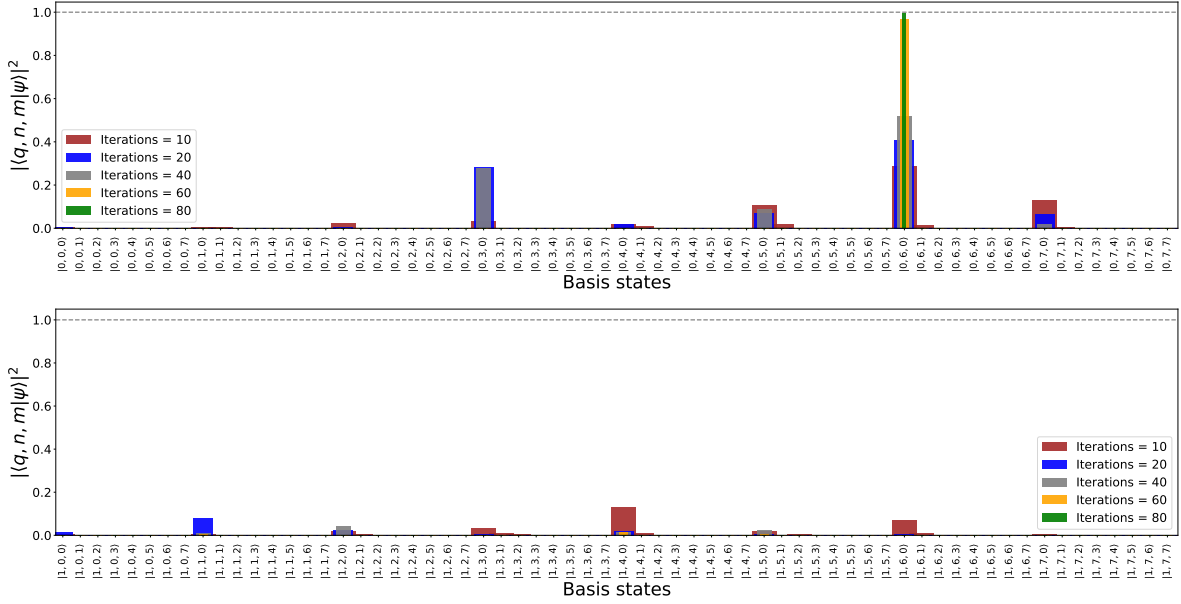


FIG. 5. Probabilities $S_{q,n,m} = |\langle q, n, m | \psi \rangle|^2$ at different numbers of iterations of the ECD-VQE method for the one-qubit two-qumode Hamiltonian H_Q defined in Eq. (25). The histograms are split into two parts for better readability of the basis states. The circuit depth for the trial state is $N_d = 5$. The corresponding trial energy values are shown in Figure 4.

The goal in traditional VQE approaches is usually to find highly accurate ground state energies whereas our goal here is to resolve the ground state $|0, 6, 0\rangle$ which represents the optimal solution. We plot the corresponding $\{S_{q,n,m}\}$ probability values as defined in Eq. (17) during different iterations of ECD-VQE in Figure 5. The ground state is practically resolved after 80 iterations and emerges as the highest peak even in 10 iterations, as shown in Figure 5. Thus, resolving the ground state may be achieved using a relatively smaller number of classical optimization steps than for finding the energy. We highlight that the $\{S_{q,n,m}\}$ probability values are directly available from photon number and Pauli-Z measurement histograms without the need for explicitly iterating over all possible integer strings such as in a classical simulator.

We also compare our results for this BKP problem with the quantum approximate optimization algorithm (QAOA)^{13,14}, which is a qubit-only VQA algorithm widely used as a benchmark quantum algorithm for combinatorial binary optimization problems. QAOA can be thought of as a special case of VQE, where the PQC ansatz consists of the alternating application of p -layers of parametrized “mixing” and “problem” unitaries, applied to a quantum register initialized in a uniform superposition

$$|\psi(\beta, \gamma)\rangle = e^{-i\beta_p H_M} e^{-i\gamma_p H_P} \dots e^{-i\beta_2 H_M} e^{-i\gamma_2 H_P} e^{-i\beta_1 H_M} e^{-i\gamma_1 H_P} |+\rangle^{\otimes N}. \quad (27)$$

The problem Hamiltonian H_P in this case is same as in

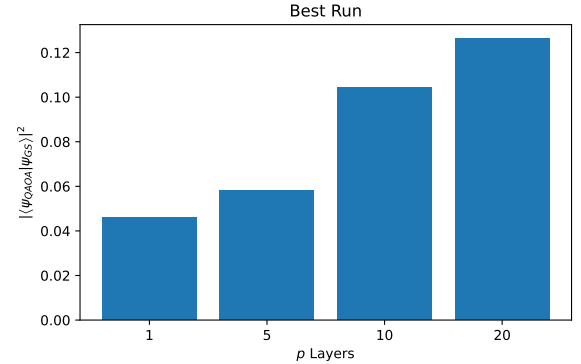


FIG. 6. Optimal probabilities for different numbers of QAOA layers chosen out of 50 independent trials for the ground state of the seven-qubit Hamiltonian defined in Eq. (25). Each trial converged with ~ 150 iterations with the classical optimizer.

Eq. (25), whereas the mixing Hamiltonian is defined as $H_M = \sum_{j=0}^{N-1} \sigma_j^x$. The QAOA calculations were implemented numerically with QuTiP using the BFGS classical optimizer. The optimal QAOA result out of 50 independent trials for increasing layers is shown in Figure 6. These results show that the probability of measuring the bitstring corresponding to the solution generally increases by increasing the number of layers. We note that the QAOA approach with $p = 20$ layers has the same number of variational parameters as the ECD-

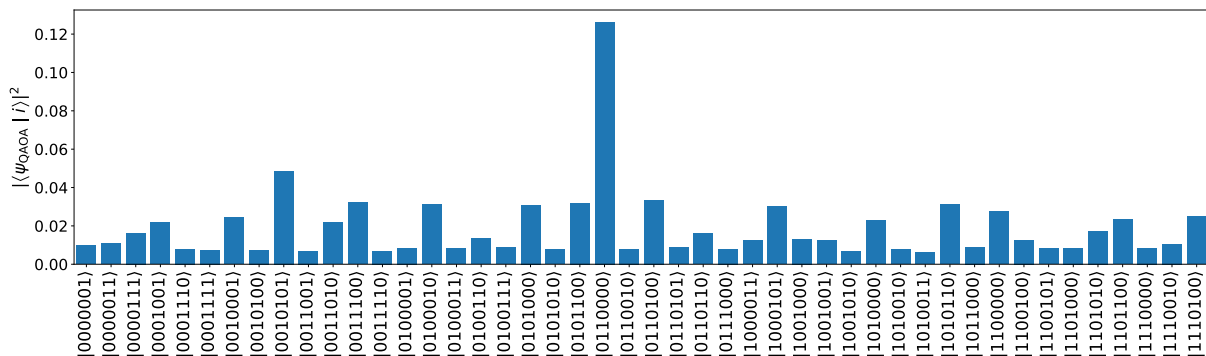


FIG. 7. Measurement probabilities for bitstring basis states for the optimal QAOA state with $p = 20$ -layers for the seven-qubit Hamiltonian defined in Eq. (25).

VQE approach with $N_d = 5$ blocks, highlighting the more favorable optimization landscape for the ECD-based approach. We also note that the number of CNOT gates per layer scales as $\mathcal{O}(N^2)$ for QUBO problems where N is the number of qubits⁵⁹. Indeed, the number of two-qubit CNOT gates needed for the BKP problem discussed here for even one layer is 42, which is more than the gate counts for the ECD-VQE approach, where $N_d = 5$ blocks correspond to only 10 one-qubit one-qumode ECD gates. Since the highest probability of measuring the solution was obtained with $p = 20$ layers, we chose to sample the measurement outcomes with this optimal QAOA circuit. The results of the measurement sampling are shown in Figure 7. Although the solution bitstring has the highest measurement probability, we see that there is still a substantial likelihood of sampling sub-optimal states. The comparison between Figure 5 and Figure 7 indicates the potential advantages of an expressive VQE ansatz over the QAOA approach whose ansatz is limited by its cost and mixing Hamiltonians. In our case, the VQE ansatz is provided by a set of native qubit-qumode gates that reveal the optimal solutions with the help of a few blocks of gates. Mimicking the ECD-VQE ansatz on a qubit-only device will lead to a deep circuit^{30,46}, which motivates our VQE approach with hybrid qubit-qumode hardware.

B. Multiple constraints

Our approach can be applied to any constrained optimization problem beyond the BKP problem discussed above. Indeed, let us discuss another simple constrained optimization problem given below

$$\min_{\mathbf{x}} x_0 + 2x_1 + x_2, \quad (28a)$$

$$\text{subject to } x_0 + x_1 = 1, \quad (28b)$$

$$2x_0 + 2x_1 + x_2 \leq 3, \quad (28c)$$

$$x_0 + x_1 + x_2 \geq 1. \quad (28d)$$

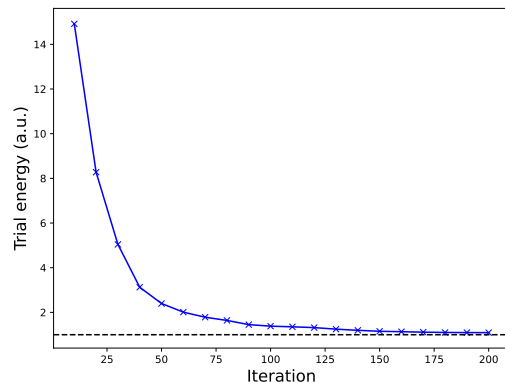


FIG. 8. Trial energy values defined in Eq. (15) at different ECD-VQE iterations while finding the ground state of H_Q defined in Eq. (30). The horizontal black line represents the exact ground state energy. The circuit depth for the trial state is $N_d = 10$.

which can be represented as the following QUBO problem

$$\begin{aligned} \min_{\mathbf{x}} F = & x_0 + x_1 + x_2 + \lambda_1 (1 - x_0 - x_1)^2 \\ & + \lambda_2 [3 - (2x_0 + 2x_1 + x_2) - (x_3 + 2x_4)]^2 \\ & + \lambda_3 [(x_0 + x_1 + x_2) - x_5 - 1]^2, \end{aligned} \quad (29)$$

consisting of $3 + 3 = 6$ binary variables. For the penalty weight $\lambda = 5$, the corresponding six-qubit Hamiltonian is given by

$$\begin{aligned} H_Q = & 32.0 - 10.5 Z_0 - 11.0 Z_1 - 5.5 Z_2 - 5.0 Z_3 \\ & - 10.0 Z_4 + 15.0 Z_0 Z_1 + 7.5 Z_0 Z_2 + 5.0 Z_0 Z_3 \\ & + 10.0 Z_0 Z_4 - 2.5 Z_0 Z_5 + 7.5 Z_1 Z_2 + 5.0 Z_1 Z_3 \\ & + 10.0 Z_1 Z_4 - 2.5 Z_1 Z_5 + 2.5 Z_2 Z_3 + 5.0 Z_2 Z_4 \\ & - 2.5 Z_2 Z_5 + 5.0 Z_3 Z_4. \end{aligned} \quad (30)$$

The ground state of H_Q obtained by exact diagonalization is $|1, 0, 0\rangle_Q \otimes |1, 0, 0\rangle_Q$ with eigenvalue 1. Indeed,

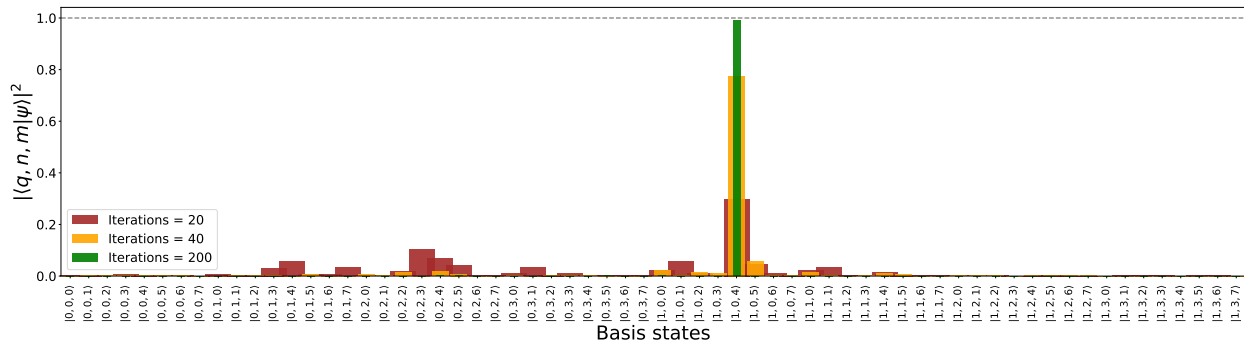


FIG. 9. Probabilities $S_{q,n,m} = |\langle q, n, m | \psi \rangle|^2$ at different numbers of iterations of the ECD-VQE method for the one-qubit two-qumode Hamiltonian H_Q defined in Eq. (30). The circuit depth for the trial state is $N_d = 10$. The corresponding trial energy values are shown in Figure 8.

the optimal solution is $\mathbf{x}^* = (1, 0, 0)$. Let us now reorganize the Hilbert space of the six-qubit Hamiltonian into three parts such that it will be mapped to a one-qubit two-qumode system with the Fock cutoffs for the two qumodes being $L_1 = 4$ and $L_2 = 8$. In other words, we map the first three qubits corresponding to the primary variables to the qubit along with the first qumode, and the rest to the second qumode. The ground state of H_Q is now mapped as

$$|1, 0, 0\rangle_Q \otimes |1, 0, 0\rangle_Q \leftrightarrow |1\rangle_Q \otimes |0\rangle_C \otimes |4\rangle_C, \quad (31)$$

or in shorthand, $|1, 0, 4\rangle$ will be our target state for the ECD-VQE approach as before.

We show the trial energies for the ECD-VQE method applied to H_B of Eq. (30) in Figure 8 and the corresponding overlaps in Figure 9. The circuit depth chosen for the trial state is $N_d = 10$. It is clear that the ground state of the Hamiltonian is fairly resolved after 40 iterations and emerges as the highest peak even in 20 iterations, as shown in Figure 9, even though there is space for the trial energy to converge to lower values even after 200 iterations. This again shows the efficiency of this method in resolving the optimal solution state with just a few optimization iterations.

IV. EFFECTS OF QUMODE NOISE

The implementations of the qumode circuits followed by photon number measurements discussed in this work are affected by noise in a realistic hardware setup. The dominant noise source for microwave resonators in cQED is amplitude damping via photon loss, represented by the rate equation below³⁰

$$\frac{d}{d\tau} \langle \hat{n} \rangle = -\kappa \langle \hat{n} \rangle, \quad (32)$$

where τ is time and κ is the photon loss rate. The transformation of a qumode density matrix ρ due to the amplitude damping quantum channel can be represented by

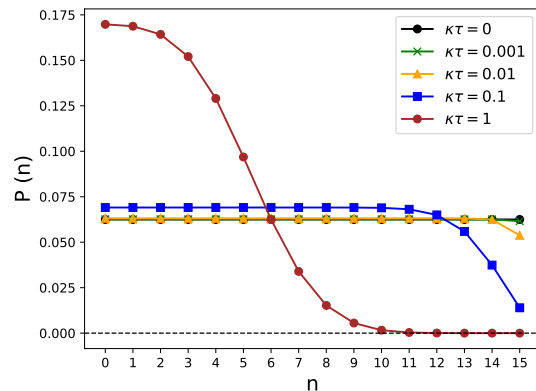


FIG. 10. Effect of amplitude damping as defined in Eq. (34) on the probabilities $P(n)$ of finding the qumode state $|n\rangle$. The initial state ρ is in an equal superposition state with a Fock cutoff of $L = 16$, which then gets modified due to Eq. (33) before simulating the photon number measurements.

the Kraus operator formalism as⁶⁰

$$\tilde{\rho} = \sum_{j=0}^{L-1} K_j \rho K_j^\dagger, \quad (33)$$

where L is the Fock cutoff for the qumode and the Kraus operators can be shown as⁶¹

$$K_j = \sqrt{\frac{(1 - e^{-\kappa\tau})^j}{j!}} e^{-\frac{\kappa\tau}{2}\hat{n}} \hat{a}^j. \quad (34)$$

Due to the truncated expression of Eq. (33), the K_0 operator must also be modified as below

$$\tilde{K}_0 = \left(\mathbb{I} - \sum_{j=1}^{L-1} K_j^\dagger K_j \right)^{1/2}, \quad (35)$$

so that the transformation remains trace-preserving³⁰. The modified photon number probabilities for a qumode

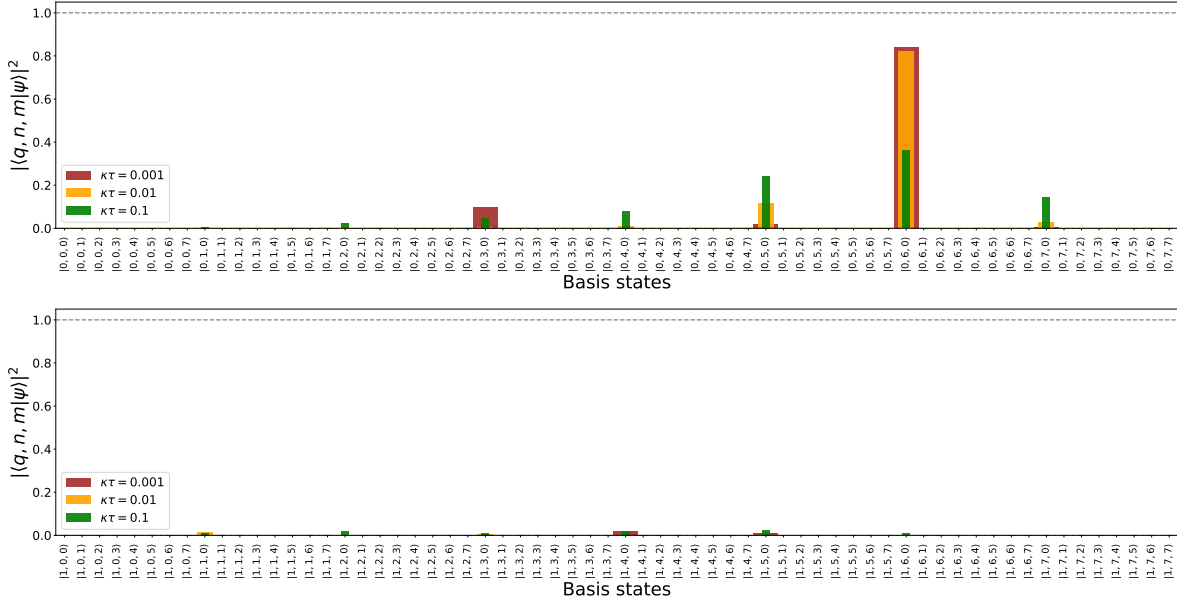


FIG. 11. Effect of qumode amplitude damping as defined in Eq. (36) on the photon number probabilities during the ECD-VQE optimization for the BKP problem defined in Eq. (25). The results are for circuit depth $N_d = 5$ with number of iterations = 80. The histograms are split into two parts for better readability of the basis states. The histograms for different noise parameters $\kappa\tau$ are plotted with different widths for better distinguishability. The corresponding noiseless results are shown in Figure 5.

can now be written as, $P(n) = \text{Tr}(|n\rangle\langle n|\tilde{\rho})$. As an example, we show how amplitude damping defined in Eq. (33) affects photon number measurements for an initial qumode state where each Fock basis state has equal amplitudes in Figure 10.

We discuss how photon loss in the qumodes will affect the ECD-VQE optimizations by applying them to the BKP example discussed in Section III A below. The density matrix ρ transformation from the noise channel can be represented as

$$\tilde{\rho} = \sum_{j=0}^{L_1-1} \sum_{k=0}^{L_2-1} (\mathbb{I} \otimes K_j \otimes K_k) \rho (\mathbb{I} \otimes K_j^\dagger \otimes K_k^\dagger), \quad (36)$$

where we have assumed the photon loss rate κ is the same for each of the qumodes and ignored the noise on the qubit. We assume that the noise channels affect the quantum state after each block of ECD with qubit rotation block U_{ER} defined in Eq. (22) is applied, i.e., the time parameter τ in Eq. (34) will be the circuit execution time for each U_{ER} block. After each unitary block is applied, we can represent the updated density matrix as, $\rho \leftarrow U_{ER} \rho U_{ER}^\dagger$, which then undergoes the noise channel transformation as defined in Eq. (36). We show the effects of photon loss on the ECD-VQE optimization for the BKP problem in Eq. (25) in Figure 11, where we plotted the photon number probabilities after 80 iterations. For the noiseless case, 80 iterations are enough to get a resolved peak, as shown in Figure 5. This is also

the case up to $\kappa\tau = 0.01$, where the optimization can also resolve the correct solution $|0, 6, 0\rangle$ with certainty. However, the optimization performance starts to deteriorate around $\kappa\tau = 0.1$. Thus, Figure 11 gives us an estimate of how the photon loss rate must relate to the implementation time for qubit-qumode on a real quantum device, which is represented by the $\kappa\tau < 0.1$ regime.

V. DISCUSSIONS

We have introduced a variational quantum algorithm for optimization problems using a qubit-qumode device that can be applied to constrained optimization problems using their QUBO form. Our approach replaces the need for many qubits with only two qumodes coupled to one qubit, which can be implemented using two microwave cavities coupled to a transmon qubit. Generalization of our approach to multiple qumodes is straightforward which can allow mapping an arbitrary number of qubits to a few qumodes. We have applied our method to a benchmark binary knapsack problem, where the seven qubits representing the seven variables are mapped to one qubit and two qumodes. We have also applied this method to an optimization problem with multiple constraints corresponding to a six-qubit Hamiltonian.

The ECD-VQE approach that we discuss requires simply running the qubit-qumode circuit and measuring it in their combined Hilbert space basis for computing the

expectation values. Furthermore, the measurements are sufficient to resolve the optimal solution, even if the cost function value did not strictly converge to the exact ground state energy. This potentially allows a smaller number of iterations that are needed for resolving the optimal solution relative to the traditional VQE approaches, thus allowing our approach to go beyond the limitations of classical optimization heuristics⁶². Even with two qumodes, our approach can be extended to problems with more binary variables based on the Fock cutoff realized by the hardware.

The Hilbert space mapping approach discussed in Section II B can be applied to any multi-qubit Hamiltonian with diagonal terms, i.e., terms involving only Pauli-Z and identity operators. Thus, our approach applies to any QUBO problem that is first mapped into a qubit Hamiltonian before representing it in terms of the Hilbert space of a composite one-qubit multi-qumode system. Specifically, R number of qumodes coupled to one qubit is equivalent to the number of qubits $N = 1 + \lceil \log_2(\prod_{j=1}^R L_j) \rceil$, where $\{L_j\}$ are the Fock cutoffs for the qumodes. This is a significant resource reduction going from a qubit-centric architecture to the hybrid qubit-qumode approach with the flexibility of increasing the number of qumodes or Fock cutoffs based on the hardware resource.

We have mostly focused on implementing the ECD-VQE method with a noiseless simulator to highlight the novelty of this approach. We have briefly discussed the effect of photon loss in the resonator qumode, the dominant noise source in a realistic cQED setup, on the optimization in Section IV. The photon loss rate and ECD gate implementation times are currently in the same

timescale¹⁶. Quantum error correction (QEC) applied to Fock states of qumodes beyond the first two levels can resolve the noise error^{63–65}, which is a challenge for near-term hardware. Nevertheless, huge progress has been recently made in demonstrating error-corrected logical qubits using qumode resonators beyond break-even⁴⁴, and extended for Fock levels of qumodes as well⁴⁵. One promising approach with contemporary hardware to tackle the photon loss noise is quantum error mitigation (QEM) techniques, which manage errors on noisy quantum devices. Multiple QEM strategies have been developed for qumode photon loss^{66–69}, and we leave the combination of these approaches with our ECD-VQE method as future work.

ACKNOWLEDGMENTS

The authors acknowledge partial support from the National Science Foundation Engines Development Award: Advancing Quantum Technologies (CT) under Award Number 2302908. VSB acknowledges partial support from Boehringer Ingelheim and from the NSF Center for Quantum Dynamics on Modular Quantum Devices (CQD-MQD) under grant number 2124511. CW acknowledges partial support from the Department of Energy (Grant No. DE-SC0025521).

CODE AND DATA AVAILABILITY

The Python code and data for the optimizations can be found at https://github.com/CQDMQD/codes_qumode_qubo.

-
- ¹ J. R. McClean, J. Romero, R. Babbush, and A. Aspuru-Guzik, *New J. Phys.* **18**, 023023 (2016).
- ² M. Cerezo, A. Arrasmith, R. Babbush, S. C. Benjamin, S. Endo, K. Fujii, J. R. McClean, K. Mitarai, X. Yuan, L. Cincio, *et al.*, *Nat. Rev. Phys.* **3**, 625 (2021).
- ³ J. Tilly, H. Chen, S. Cao, D. Picozzi, K. Setia, Y. Li, E. Grant, L. Wossnig, I. Rungger, G. H. Booth, *et al.*, *Phys. Rep.* **986**, 1 (2022).
- ⁴ A. Callison and N. Chancellor, *Phys. Rev. A* **106**, 010101 (2022).
- ⁵ K. Yawata, Y. Osakabe, T. Okuyama, and A. Asahara, in *2022 IEEE International Conference on Big Data (Big Data)* (IEEE, 2022) pp. 2437–2440.
- ⁶ A. Ajagekar and F. You, *npj Comput. Mater.* **9**, 143 (2023).
- ⁷ T. Zaborniak, J. Giraldo, H. Müller, H. Jabbari, and U. Stege, in *2022 IEEE International Conference on Quantum Computing and Engineering (QCE)* (IEEE, 2022) pp. 174–185.
- ⁸ K. Yanagisawa, T. Fujie, K. Takabatake, and Y. Akiyama, *Entropy* **26**, 397 (2024).
- ⁹ P. Date, D. Arthur, and L. Pusey-Nazzaro, *Sci. Rep.* **11**, 10029 (2021).
- ¹⁰ T. Matsumori, M. Taki, and T. Kadowaki, *Sci. Rep.* **12**, 12143 (2022).
- ¹¹ S. Feld, C. Roch, T. Gabor, C. Seidel, F. Neukart, I. Galter, W. Mauerer, and C. Linnhoff-Popien, *Frontiers in ICT* **6**, 13 (2019).
- ¹² D. Laughhunn, *Oper. Res.* **18**, 454 (1970).
- ¹³ E. Farhi, J. Goldstone, and S. Gutmann, arXiv preprint arXiv:1411.4028 (2014).
- ¹⁴ K. Blekos, D. Brand, A. Ceschini, C.-H. Chou, R.-H. Li, K. Pandya, and A. Summer, *Phys. Rep.* **1068**, 1 (2024).
- ¹⁵ A. Peruzzo, J. McClean, P. Shadbolt, M.-H. Yung, X.-Q. Zhou, P. J. Love, A. Aspuru-Guzik, and J. L. O’Brien, *Nat. Commun.* **5**, 4213 (2014).
- ¹⁶ A. Eickbusch, V. Sivak, A. Z. Ding, S. S. Elder, S. R. Jha, J. Venkatraman, B. Royer, S. M. Girvin, R. J. Schoelkopf, and M. H. Devoret, *Nat. Phys.* **18**, 1464 (2022).
- ¹⁷ X. You, Y. Lu, T. Kim, D. M. Kurkuoglu, S. Zhu, D. van Zanten, T. Roy, Y. Lu, S. Chakram, A. Grassellino, A. Romanenko, J. Koch, and S. Zorzetti, arXiv preprint arXiv:2403.00275 (2024).
- ¹⁸ B. Zhang and Q. Zhuang, *Quantum Sci. Technol.* **10**, 015009 (2024).

- ¹⁹ R. A. Quintero and L. F. Zuluaga, Techn. Ber. Technical Report. Department of Industrial and Systems Engineering, Lehigh University (2021).
- ²⁰ T. Bontekoe, F. Phillipson, and W. v. d. Schoot, in *International Conference on Computational Science* (Springer, 2023) pp. 90–107.
- ²¹ S. Martello and P. Toth, *Knapsack problems: Algorithms and computer implementations* (John Wiley & Sons, 1990).
- ²² M. Willsch, D. Willsch, F. Jin, H. De Raedt, and K. Michielsen, *Quantum Inf. Process.* **19**, 1 (2020).
- ²³ J. Rajakumar, J. Golden, A. Bärtschi, and S. Eidenbenz, in *Proceedings of the 21st ACM International Conference on Computing Frontiers* (2024) pp. 199–206.
- ²⁴ S. Singhal, V. Srivastava, P. Rohith, P. Jain, and D. Bhowmik, in *2024 8th IEEE Electron Devices Technology & Manufacturing Conference (EDTM)* (IEEE, 2024) pp. 1–3.
- ²⁵ T. Müller, A. Singh, F. K. Wilhelm, and T. Bode, arXiv preprint arXiv:2411.19388 (2024).
- ²⁶ A. Blais, A. L. Grimsmo, S. M. Girvin, and A. Wallraff, *Rev. Mod. Phys.* **93**, 025005 (2021).
- ²⁷ T. J. Stavenger, E. Crane, K. C. Smith, C. T. Kang, S. M. Girvin, and N. Wiebe, in *2022 IEEE High Performance Extreme Computing Conference (HPEC)* (IEEE, 2022) pp. 1–8.
- ²⁸ A. Copetudo, C. Y. Fontaine, F. Valadares, and Y. Y. Gao, *Appl. Phys. Lett.* **124**, 080502 (2024).
- ²⁹ R. Dutta, D. G. Cabral, N. Lyu, N. P. Vu, Y. Wang, B. Allen, X. Dan, R. G. Cortiñas, P. Khazaei, S. E. Smart, *et al.*, *J. Chem. Theory Comput.* **20**, 6426 (2024).
- ³⁰ Y. Liu, S. Singh, K. C. Smith, E. Crane, J. M. Martyn, A. Eickbusch, A. Schuckert, R. D. Li, J. Sinanan-Singh, M. B. Soley, *et al.*, arXiv preprint arXiv:2407.10381 (2024).
- ³¹ E. Crane, K. C. Smith, T. Tomesh, A. Eickbusch, J. M. Martyn, S. Kühn, L. Funcke, M. A. DeMarco, I. L. Chuang, N. Wiebe, *et al.*, arXiv preprint arXiv:2409.03747 (2024).
- ³² J. Y. Araz, M. Grau, J. Montgomery, and F. Ringer, arXiv preprint arXiv:2410.07346 (2024).
- ³³ C. Weedbrook, S. Pirandola, R. García-Patrón, N. J. Cerf, T. C. Ralph, J. H. Shapiro, and S. Lloyd, *Rev. Mod. Phys.* **84**, 621 (2012).
- ³⁴ G. Verdon, J. M. Arrazola, K. Brádler, and N. Killoran, arXiv preprint arXiv:1902.00409 (2019).
- ³⁵ Y. Enomoto, K. Anai, K. Udagawa, and S. Takeda, *Phys. Rev. Res.* **5**, 043005 (2023).
- ³⁶ F. Khosravi, A. Scherer, and P. Ronagh, in *2023 IEEE International Conference on Quantum Computing and Engineering (QCE)*, Vol. 1 (IEEE, 2023) pp. 184–195.
- ³⁷ P. Chandarana, K. Paul, M. Garcia-de Andoin, Y. Ban, M. Sanz, and X. Chen, *Commun. Phys.* **7**, 315 (2024).
- ³⁸ J. L. O’Brien, A. Furusawa, and J. Vučković, *Nat. Photonics* **3**, 687 (2009).
- ³⁹ J. Wang, F. Sciarrino, A. Laing, and M. G. Thompson, *Nat. Photonics* **14**, 273 (2020).
- ⁴⁰ J. M. Arrazola, V. Bergholm, K. Brádler, T. R. Bromley, M. J. Collins, I. Dhand, A. Fumagalli, T. Gerrits, A. Goussev, L. G. Helt, *et al.*, *Nature* **591**, 54 (2021).
- ⁴¹ K. Marshall, R. Pooser, G. Siopsis, and C. Weedbrook, *Phys. Rev. A* **91**, 032321 (2015).
- ⁴² S. Krastanov, V. V. Albert, C. Shen, C.-L. Zou, R. W. Heeres, B. Vlastakis, R. J. Schoelkopf, and L. Jiang, *Phys. Rev. A* **92**, 040303 (2015).
- ⁴³ A. A. Diringer, E. Blumenthal, A. Grinberg, L. Jiang, and S. Hacohe-Gourgy, *Phys. Rev. X* **14**, 011055 (2024).
- ⁴⁴ V. Sivak, A. Eickbusch, B. Royer, S. Singh, I. Tsioutsios, S. Ganjam, A. Miano, B. Brock, A. Ding, L. Frunzio, *et al.*, *Nature* **616**, 50 (2023).
- ⁴⁵ B. L. Brock, S. Singh, A. Eickbusch, V. V. Sivak, A. Z. Ding, L. Frunzio, S. M. Girvin, and M. H. Devoret, arXiv preprint arXiv:2409.15065 (2024).
- ⁴⁶ C. S. Wang, J. C. Curtis, B. J. Lester, Y. Zhang, Y. Y. Gao, J. Freeze, V. S. Batista, P. H. Vaccaro, I. L. Chuang, L. Frunzio, L. Jiang, S. M. Girvin, and R. J. Schoelkopf, *Phys. Rev. X* **10**, 021060 (2020).
- ⁴⁷ R. Dutta, N. P. Vu, C. Xu, D. Cabral, N. Lyu, A. V. Soudackov, X. Dan, H. Li, C. Wang, and V. S. Batista, arXiv preprint arXiv:2404.10222 (2024).
- ⁴⁸ S. Martello and P. Toth, *Oper. Res.* **45**, 768 (1997).
- ⁴⁹ S. Martello, D. Pisinger, and P. Toth, *Manag. Sci.* **45**, 414 (1999).
- ⁵⁰ D. Pisinger, *Comput. Oper. Res.* **32**, 2271 (2005).
- ⁵¹ H. M. Salkin and C. A. De Kluyver, *Nav. Res. Logist. Q.* **22**, 127 (1975).
- ⁵² I. Yevseyeva, E. B. Lenseink, A. de Vries, A. P. IJzerman, A. H. Deutz, and M. T. Emmerich, *Inf. Sci.* **475**, 29 (2019).
- ⁵³ Y. Wang, Z. Hu, B. C. Sanders, and S. Kais, *Front. Phys.* **8**, 589504 (2020).
- ⁵⁴ N. Metropolis, A. W. Rosenbluth, M. N. Rosenbluth, A. H. Teller, and E. Teller, *J. Chem. Phys.* **21**, 1087 (1953).
- ⁵⁵ W. K. Hastings, *Biometrika* **57**, 97 (1970).
- ⁵⁶ N. Mohseni, P. L. McMahon, and T. Byrnes, *Nat. Rev. Phys.* **4**, 363 (2022).
- ⁵⁷ J. R. Johansson, P. D. Nation, and F. Nori, *Comput. Phys. Commun.* **183**, 1760 (2012).
- ⁵⁸ P. Virtanen, R. Gommers, T. E. Oliphant, M. Haberland, T. Reddy, D. Cournapeau, E. Burovski, P. Peterson, W. Weckesser, J. Bright, *et al.*, *Nat. Methods* **17**, 261 (2020).
- ⁵⁹ J. Weidenfeller, L. C. Valor, J. Gacon, C. Tornow, L. Bello, S. Woerner, and D. J. Egger, *Quantum* **6**, 870 (2022).
- ⁶⁰ M. A. Nielsen and I. L. Chuang, *Quantum computation and quantum information* (Cambridge university press, 2010).
- ⁶¹ M. H. Michael, M. Silveri, R. T. Brierley, V. V. Albert, J. Salmilehto, L. Jiang, and S. M. Girvin, *Phys. Rev. X* **6**, 031006 (2016).
- ⁶² S. Lee, J. Lee, H. Zhai, Y. Tong, A. M. Dalzell, A. Kumar, P. Helms, J. Gray, Z.-H. Cui, W. Liu, *et al.*, *Nat. Commun.* **14**, 1952 (2023).
- ⁶³ K. Noh, S. Girvin, and L. Jiang, *Physical Review Letters* **125**, 080503 (2020).
- ⁶⁴ J. Wu, A. J. Brady, and Q. Zhuang, *Quantum* **7**, 1082 (2023).
- ⁶⁵ S. Dutta, D. Biswas, and P. Mandayam, arXiv preprint arXiv:2406.02444 (2024).
- ⁶⁶ D. Su, R. Israel, K. Sharma, H. Qi, I. Dhand, and K. Brádler, *Quantum* **5**, 452 (2021).
- ⁶⁷ A. Taylor, G. Bressanini, H. Kwon, and M. Kim, *Phys. Rev. A* **110**, 022622 (2024).
- ⁶⁸ J. Mills and R. Mezher, arXiv preprint arXiv:2405.02278 (2024).
- ⁶⁹ Y. Teo, S. Shringarpure, S. Cho, and H. Jeong, arXiv preprint arXiv:2411.11313 (2024).